Materials Horizons

Functional mapping reveals mechanistic clusters for OER catalysis across (Cu-Mn-Ta-Co-Sn-Fe)Ox composition and pH space

Journal:	*Materials Horizons*
Manuscript ID	MH-COM-12-2018-001641.R1
Article Type:	Communication
Date Submitted by the Author:	18-Mar-2019
Complete List of Authors:	Stein, Helge; California Institute of Technology, Joint Center for Artificial Photosynthesis Guevarra, Dan; California Institute of Technology Shinde, Aniketa; California Institute of Technology Jones, Ryan; California Institute of Technology, Joint Center for Artificial Photosynthesis; Joint Center for Artificial Photosy, Gregoire, John; California Institute of Technology, Joint Center for Artificial Photosynthesis Haber, Joel; California Institute of Technology, Joint Center for Artificial Photosynthesis; California Institute of Technology

Conceptual insights

Combinatorial science and high throughput experimentation via instrument automation is producing unprecedented quantities of experimental data. The high dimensionality and large volume of these datasets now exceeds human ability to simultaneously comprehend the full dataset. Herein we demonstrate the utility of multi-dimensional scaling methods to facilitate the use of human intuition and understanding in the analysis of large data sets as applied to the pH-dependent oxygen evolution electrocatalytic activity of 2121 multi-metal oxide compositions spanning 15 pseudo-quaternary composition spaces. Combined with additional clustering analysis, three distinct classes of OER catalysts are identified as well as a compositionally tuneable catalyst family enabling high performance in acidic and neutral pHs.

Journal Name

ARTICLE

Functional mapping reveals mechanistic clusters for OER catalysis across (Cu-Mn-Ta-Co-Sn-Fe)O_x composition and pH space.

Received 00th January 20xx,
Accepted 00th January 20xx

DOI: 10.1039/x0xx00000x

www.rsc.org/

Helge S. Stein[1], Dan Guevarra[1], Aniketa Shinde[1], Ryan J. R. Jones[1], John M. Gregoire[1], Joel A. Haber[1*]*

Identification of stable electrocatalysts for the oxygen evolution reaction (OER) remains a primary challenge in materials for energy. The pH-dependent activity is known for very few catalysts, prompting our exploration of a broad range of catalysts using high throughput experiments and data science. This approach enables the largest screening of OER activity and operational stability to date, as illustrated through investigation of the (Cu-Mn-Ta-Co-Sn-Fe)O_x composition space as 15 unique quaternary composition spaces. In total 2121 compositions are tested between pH 3 and 13, creating an extensive dataset whose interpretation requires development and application of data science to provide insights that are both beyond the standard composition-activity relationships and beyond human interpretation due to the dimensionality of the dataset. Three distinct classes of OER catalysts are identified with respect to pH-dependent activity and stability. The large-scale screening reveals a new class of Co-rich OER catalysts that can be compositionally tailored to a specified pH and perform on par with state-of-the-art acid OER catalysts.

Introduction

Solar fuels generation by means of harvesting sunlight to generate hydrogen or carbon-containing fuels as a renewable energy carrier is a promising technology for meeting future energy needs.[1,2] However, technologies based on water splitting as well as CO_2 reduction are limited in efficiency by the activity and stability of OER catalysts.[1,3,4] Direct utilization of solar energy for OER involves development of a photoanode, whose operational pH is typically determined by device considerations and the stability requirements of the light-harvesting semiconductor.[5,6] The photoanode also typically requires an OER catalyst coating, and initial reports indicate that the performance of light absorbers with and without catalyst coatings strongly depend on electrolyte pH.[7–9] Indeed, several recent publications indicate that the fundamental mechanism for OER on a particular catalyst composition may change as a function of electrolyte pH as a result of pH-dependent metal center oxidation states, surface speciation, and surface charge. The continued discovery of photoanode light absorbers that operate in different electrolyte pH motivates the design of OER catalysts that provide the requisite activity and stability under the specific operating conditions[8]. Studying composition-dependent changes in activity and stability can yield general design rules and/or functional classes of materials, i.e. materials serving specialized tasks that exhibit qualitatively different functional behaviors like acid- or alkaline-active catalysis[10–14].

Prior high-throughput experimental search campaigns for identifying metal oxide OER catalysts in high-order composition spaces (containing up to 4 cations) by our group indicate that 10 at.% is an appropriate composition interval for sampling such composition spaces, and that unique performance can emerge with different combinations of cations.[15,16] While this approach enables identification of composition-activity trends within a given 3- or 4-cation space, a more global mapping of such trends is demonstrated in the present work by exploring higher dimensional composition and electrolyte spaces by varying both to provide an in-depth functional assessment.

To accelerate catalyst exploration over diverse metal oxide composition spaces, a new composition library design was developed to synthesize, on a single plate, all unique compositions containing 1, 2, 3 or 4 cations with 10 at.% intervals for a set of 6 elements, corresponding to the simultaneous synthesis of the 2121 unique compositions needed to cover all 15 pseudo-quaternary composition spaces. Previous work on ink-jet printed and sputtered OER catalysts also indicates that a calcination temperature high enough to convert the precursors to metal oxides and low enough to mitigate particle sintering provides the highest activity,[4,17–19] so processing was fixed to a single annealing temperature of

[a] *Joint Center for Artificial Photosynthesis, California Institute of Technology, Pasadena, California 91125, USA*

† Footnotes relating to the title and/or authors should appear here.

Electronic Supplementary Information (ESI) available: Additional experimental details, composition changes from XRF; additional HiTp analysis of (Co-Cu-Mn-Sn)O_x composition space and scaled up sample measurements of select compositions in that space at pH 3; cMDS plots of (La-Ce-Mn-Co-Ni-Fe)Ox and (Cu-Mn-Ta-Co-Ni-Fe)Ox at pHs 3, 7, 9, and 13; complete pseudo-quaternary FoM plots at pHs 3, 7, 9, and 13 for all three 6-metal oxide composition spaces. See DOI: 10.1039/x0xx00000x

400 °C. While many catalysts exhibited initial transients in their activity due to changes to the catalyst surface, these are ascribed to catalyst oxidation and formation of a corrosion passivation layer. Empirically we have observed that such transients consistently stabilize within several minutes, enabling the design of a pre-aging protocol. For catalyst loadings of 4 nmoles/mm^2, if only 1% of 10 mA cm^{-2} of anodic current during initial operation arises from catalyst corrosion, the entire catalyst would corrode in ~60 minutes. Therefore, 120 minutes of operation identifies catalysts that exhibit relatively stable initial operation. Since long duration measurements are not amenable to high throughput serial measurements, we perform parallel operation of the catalysts for 2 hours[20] prior to serial catalyst evaluation using established high throughput techniques.[21]

With these high throughput methodologies, the high dimensional composition-pH parameter space can be experimentally explored, yet interpretability of this data suffers from the so-called "combinatorial explosion". The combinatorial explosion describes the situation when multiple composition spaces (here 15 psuedo-quaternaries) in different environments (here four pHs) produces large numbers (here 60) scalar performance maps over high-order composition spaces (here pseudo-quaternary composition spaces), as presented in Figure S8 of the ESI for the (Cu-Mn-Ta-Co-Sn-Fe)O_x composition space data. This volume of data, even with advanced visualization schemes from combinatorial materials science,[22–24] exceeds the ability of most human minds to digest, and if expanded to multiple six-metal oxide compositions clearly is too great to fully comprehend (See the ESI for such figure of merit plots for the additional composition spaces (Cu-Mn-Ta-Co-Ni-Fe)O_x and (La-Ce-Mn-Co-Ni-Fe)O_x.

It was therefore concluded that the generation of scientific insights and discovery of new materials for OER is limited by the rate of assessing 'classic' visualization methods. Based on Li et al.[25] we utilize multidimensional scaling (MDS) for dimensionality reduction in visualizing complex electrochemical datasets. MDS[25,26] is chosen over PCA, t-SNE[27] or other methods[22], because the interest is in preserving compositional similarity (measured as L_2-distance) in contrast to describing variance or stochastic properties of the dataset. This visualization method allows us to use human intuition and intelligence[28–30] to unravel non-linear trends in activity with composition and pH. MDS for functional maps is successfully employed in the discovery of Co-based OER catalysts that excel in maintaining activity over the range of pH 3 to 13, including high activity in acidic electrolytes.

Methods

Platemap design

In order to capitalize on the above mentioned (and other) experiences and insights we chose to design a new platemap utilizing our standard platform[15,31] (10 cm × 15 cm FTO coated substrate, with 1 mm^2 sample spots printed on a rectangular grid on a 2 mm pitch) but utilizing 6 metal oxide precursor inks for the library instead of four. The use of 6 metals produces 15 pseudo-quaternary composition spaces (6 choose 4 combinations), each of which contains 286 discrete compositions utilizing a 10 at.% composition step, for a total of 4290 samples. However, because each of the pseudo-quaternary composition spaces also contain 1, 2, and 3 metal oxide compositions which are shared by other pseudo-quaternary composition spaces, the number of unique composition samples in the 6 metal, 15 pseudo-quaternary composition spaces are reduced to 2121 samples. This number of samples can be placed on a single substrate utilizing our standard printed materials library format. The generic print file is generated as a series of samples, each composed of a mixture of 1, 2, 3, or 4 inks (from a possible 6 inks) to contain a constant total volume of ink, containing 4 nanomoles of metal oxide precursor). Different physical libraries are printed by loading six precursor inks into the printer and assigning each of six ink channels a particular color in the platemap. Different composition spaces are printed and explored by loading and assigning colors to different metal oxide precursor inks. The sample compositions were randomly distributed across the entire plate to deconvolute the impact of sample composition from location-dependent processing variations and sample crosstalk on the catalytic performance.

Synthesis description

The preparation and printing of metal oxide precursor inks for the synthesis of physical material libraries has been described in detail previously,[16,32] and in the ESI. For this investigation, each sample contains 4 nanomoles of metal per 1 mm × 1 mm sample spot. Eight or more copies of each six-metal library were printed at the same time to ensure consistency between plates as the inks and printer conditions were identical. The set of duplicate libraries were processed as described previously, and in the ESI, to a final calcination temperature of 400 °C for 10 hours.

PETS experiment description

In order to experimentally identify the sparse number of compositions which are stable in acid under OER potentials, we have previously described the engineering and experimental conditions applicable for exposing a 10 cm by 15 cm plate of ~2000 samples to similar electrochemical conditions for a period of hours.[20] This parallel electrochemical treatment system (PETS) has been deployed to discover non-precious metal OER catalysts that operate in acid.[33] The system and process have been slightly modified for the present study to accommodate the different pH conditions and electrolytes used. A single calcined library containing a 6-metal composition space was treated in the PETS system at a single pH for 2 hours. The electrolytes and buffers were chosen to be stable under OER conditions, which excluded the use of many pH buffers, as they contain organic acids which are subject to oxidation. The pHs (approximated as pH 3, 7, 9 and 13 herein) and electrolytes used are:

a. pH 2.8: 10 mM H_3PO_4/40 mM NaH_2PO_4+ 0.25 M Na_2SO_4

b. pH 6.6: 50 mM NaH_2PO_4/50 mM Na_2HPO_4 + 0.25 M Na_2SO_4
c. pH 9: borate with 0.25 M Na_2SO_4
d. pH 13: 0.1 M NaOH + 0.25 M Na_2SO_4

Microporous polypropylene frits separate the anolyte and catholyte chambers to prevent spatial artefacts due to nonuniform ionic plating on the counter electrode, and both chambers continually flow electrolyte in a recirculating fashion to ensure homogenous chemical potential exposure to each sample within the library. Each library was conditioned by a 2 h current-limited CP @ 25 mA designed to minimize spatial variations in potential due to IR losses in the substrate FTO layer.

SDC Experiment description

The scanning drop electrochemical cell (SDC) and its performance has been reported previously, along with its application for evaluating OER catalyst performance.[16,17,33] Following the 2 h PETS treatment, the library was loaded onto the SDC set-up and scanned using the same pH buffer/electrolyte as was used to pretreat it in the PETS. A 2-step chronopotentiometry (CP) measurement was conducted on each sample: 15 second CP measurement at 3 mA cm^{-2}, followed by a 15 second CP measurement at 10 mA cm^{-2}. If the potential exceeded 1 V overpotential for more than 0.5 seconds the experiment was aborted and the next measurement initiated. A single scalar value for the overpotential for each sample was obtained as the average potential over the final 8 seconds of the 10 mA cm^{-2} CP measurement. Data points greater than 1.5 standard deviations from the mean were removed before averaging.

Results

Visualization of higher composition spaces

In this study, over 16,000 data points from 15 quaternary systems at 4 different pHs needed to be visualized in a comprehensive manner. Plotting all data in pseudo-quaternary diagrams at each pH produces a nearly incomprehensible array of 60 figures, as shown in Figure S8. We utilized multidimensional scaling[26] (MDS) for sample compositions (cMDS) to reduce the dimensionality of the composition space and to enable extraction of insights from these plots. This visualization is performed similar to how quinary compositions were visualized by Li et al.[25] As there are no compositions in our dataset containing more than four cations, the composition data is directly used in the cMDS without augmentation by the complete composition space.[25]

To introduce the reader to this kind of composition visualization, all binary lines of six arbitrary elements A - F are shown in a cMDS plot in Figure 1a). It is apparent that the 3D octahedron edges are comprised of the binaries between the elements A - F. Following from the fact that the MDS derived octahedron only has 12 edges, three binary lines (A - B, F - D, C - E) need to be broken apart, as they would need to bisect the center of the octahedron, to which the algorithm assigns large dissimilarities. Since the metric MDS[26] tried to conserve "distance", these binary lines become bent outward as they are compositionally "distant" from those inside the body of the octahedron (quaternaries). Figure 1b) shows a full cMDS color-coded by the concentration of element A, indicated by an arrow. In general cMDS conserves compositional similarity over exact mapping of binary compositions (e.g. RadViz[24]).

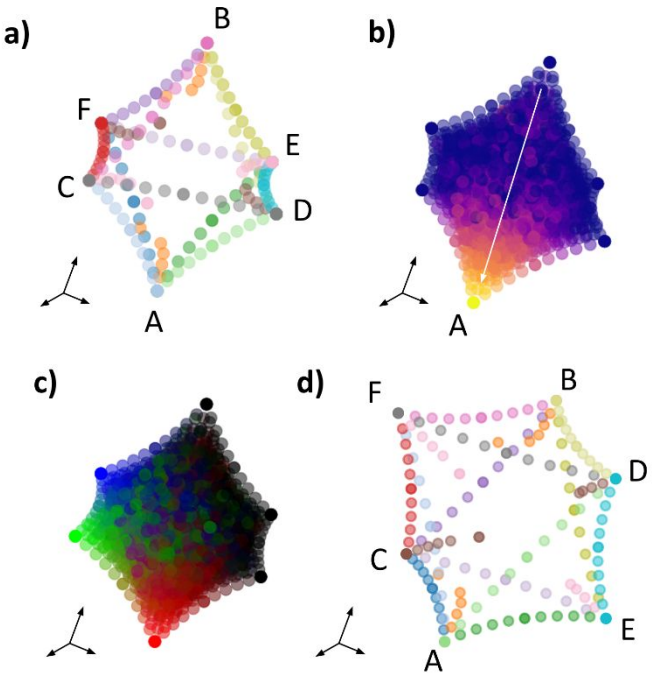

Figure 1: Visualizations of cMDS. a) cMDS with highlighted binary compositions showing that most binary composition lines are located at the edges of the 3D diamond. b) Full cMDS color coded with the content of A (purple to yellow). In general, the higher the content of A, the closer it is placed towards pure A (yellow). c) cMDS with color code according to the content of A/C/F. d) Viewing angle maximizing the distance between the pure composition endmembers used throughout the manuscript. The arrows at the left bottom indicate that these plots represent a viewing angle onto a 3D shape.

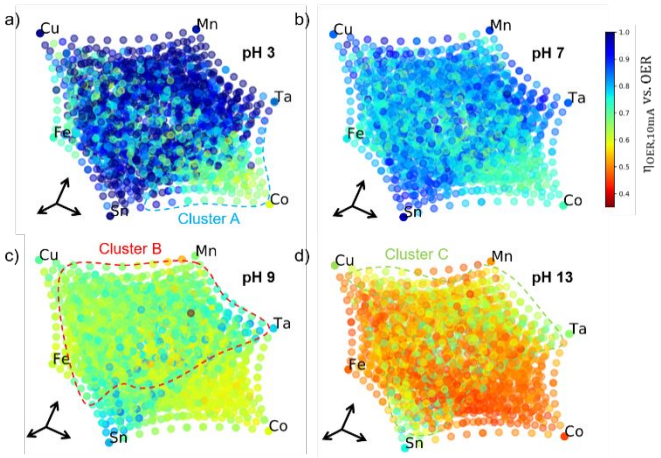

Figure 2: cMDS of (Cu-Mn-Ta-Co-Sn-Fe)O_x at pH a) 3, b) 7, c) 9, d) 13. For generating each graph a plate containing the library of composition samples was treated using PETS for 2h in the respective electrolyte and subsequently analyzed in a serial chronoamperometric measurement at 10 mA/cm^2. All graphs are color coded according to the average potential $_{OER,10mA}$ vs. OER at the respective pH to reach 10 mA/cm^2. From this visualization three functional classes become apparent: cluster I for acid active OER catalysts, cluster II for catalysts strongly reacting to changes in pH, and cluster III for bad performing (alkaline OER) catalysts.

Figure 1c) shows a full cMDS with points color coded according to their content of A/C/F as red green blue cyan (RGBC) color mapping. In Figure 1d) the viewing angle used throughout this manuscript for cMDS is shown. This viewing angle of the octahedron maximizes the visual distance between the pure elements to give readers a broader sense of trends. Where necessary, other viewing angles are shown. It should be noted that the composition of the catalysts reported is the ***intended printed compositions***, not necessarily the composition of the catalyst after PETS, as discussed below.

Pre-Aging through PETS

Corrosion of some metal oxides in the Cu-Mn-Ta-Co-Sn-Fe oxide system is expected from known Pourbaix diagrams.[34–36] In particular, Cu, Mn, and Fe oxides have limited stability at pH 3. Details are presented in the ESI of an X-ray fluorescence spectroscopy (XRF) study of composition changes to a systematic subset of compositions after electrochemical measurements were performed. This study confirms (Figure S2) that Ta was quite stable at all pHs, while many compositions had significant loss of Fe, Cu, Mn and Co after electrochemical treatment in pH 3 or 7 electrolytes. Cu was particularly stable in pH 9, but often unstable in pH 13. Interestingly, the co-presence of Cu appears to confer some corrosion stabilization to Fe at pH 9, as does the co-presence of Ta to Fe, Mn, and Co at pH 3. In addition, electrochemical treatment in specific electrolytes may change the structure of the catalysts via hydration, hydroxylation, oxidation state changes in certain metals, and incorporation of electrolyte constituents into the coating.[37–39] Thus, the nature of the catalyst post-PETS may be significantly altered from the as-calcined state and we assert more relevant to the operating catalyst performance than would be the initial performance of the as-calcined materials. However, herein we analyze the operational performance with respect to the initial composition, not a final measured composition, because the performance is also a function of the specific nanostructures and chemical structures produced by the prior history of the material. To reproduce the behavior observed, one should reproduce the initial composition and apply similar electrochemical treatments, not target the final composition obtained. This approach to using high throughput experiments to identify the samples whose detailed study will provide scientific insights has been demonstrated previously,[17,18] and the present work uses clustering and identification of representative samples to motivate a suite of future studies on the detailed compositional, microstructural, and structural-chemical characterization of the operational catalysts.

OER Activity as function of pH

OER activity was measured as the overpotential at 10 mA/cm^2 using chronopotentiometry and is shown on a common color-scale for pH 3, 7, 9, and 13 in cMDS visualizations in Figure 2. A general trend is that Co-rich samples tend to have low $\eta_{OER,10mA}$ at all pHs, with samples in the (Sn-Ta-Co)O_x region exhibiting small changes as a function of pH and samples in the (Sn-

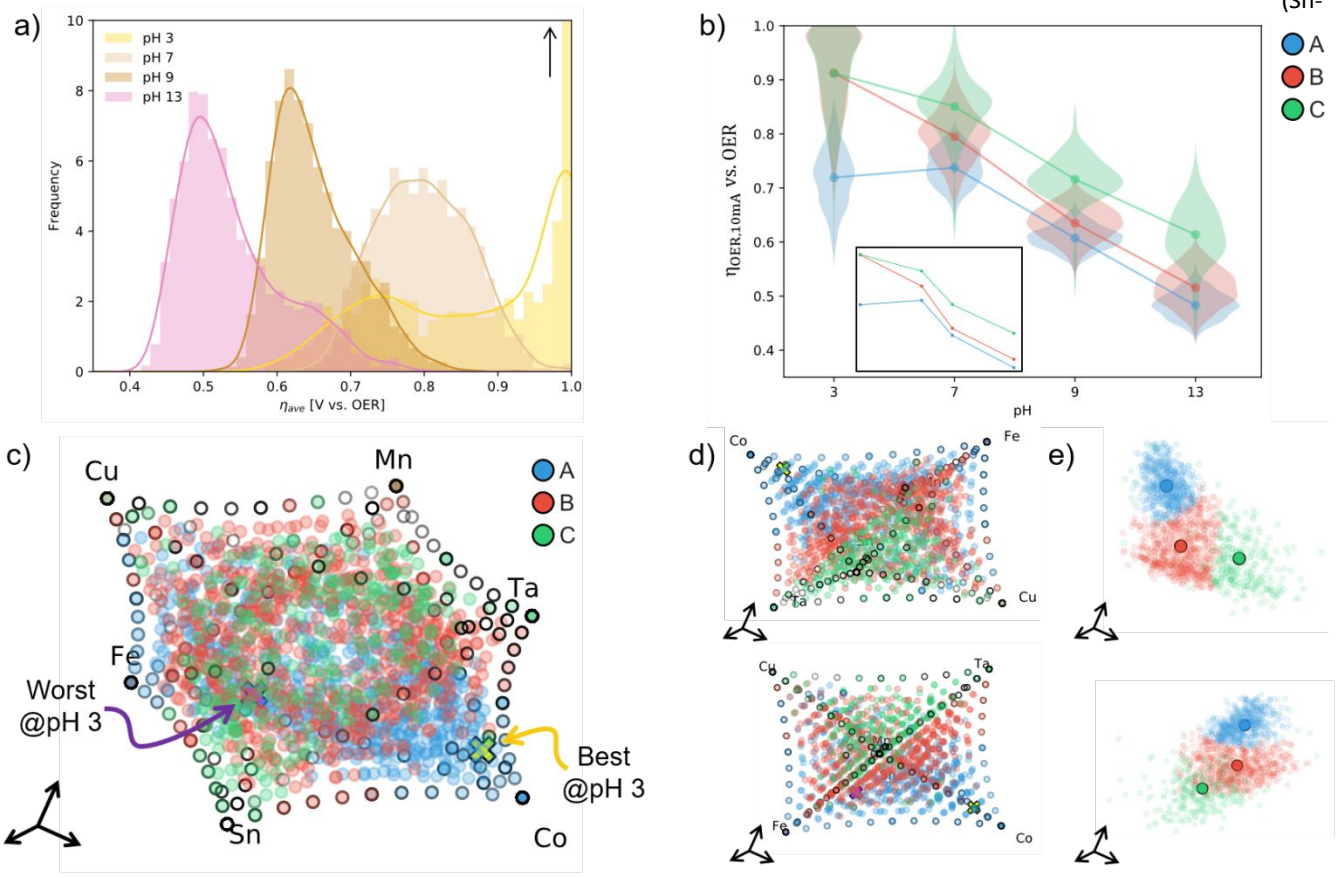

Figure 3: Histograms and *functional clustering of* $\eta_{OER,10mA}$ *vs. pH of* (Cu-Mn-Ta-Co-Sn-Fe)O_x *a) histogram of* $\eta_{OER,10mA}$ *at pH 3, 7, 9 and 13. Sample with a* $_{OER,10mA}$ *of above 1.0 V vs. OER were binned to the highest value. b) Violin plots of the different clusters identified through spectral clustering using a radial gaussian distribution kernel as affinity. c) cMDS of* $\eta_{OER,10mA}$(pH) *with cluster membership as color code, d) 2 alternate viewing angles from c and e) MDS of* $\eta_{OER,10mA/cm}$(pH) *into 3D with highlighted cluster labels and cluster kernels from 2 viewing angles.*

Cu-Mn-Ta)O_x region exhibiting large changes in $\eta_{OER,10mA}$ as a function of pH. For this composition space, the (Fe-Co)O_x-rich samples at pH 13 have the lowest $\eta_{OER,10mA}$ of all compositions at all pHs. Compositions containing more than two metals generally exhibit a lower $\eta_{OER,10mA}$ than those with two or fewer metals. Analyzing variation in $\eta_{OER,10mA}$ as a function of pH can give insight into which catalysts perform OER via different mechanisms or have different rate-limiting steps[40], this is particularly important at near-neutral pH where it is unclear whether the reactant is OH^- (the anticipated reactant in strong base) or H_2O (the anticipated reactant in strong acid). The median change in $\eta_{OER,10mA}$ with pH is -38.4 mV/pH (variance 0.54 mV/pH) which is about 2/3 of the Nernstian slope of -59.1 mV/pH (see Figure 3 a) for a histogram of the change of $\eta_{OER,10mA}$ over pH). Also, $\eta_{OER,10mA}$ changes significantly between pH 3 – 7 and between pH 9 – 13, but barely between pH 7 – 9, as can be inferred from Figure 3 a). For pH 3 many samples required more than 1 V vs. OER to achieve the current density of 10 mA cm^{-2}, which is the trigger for aborting a measurement, thus these values were binned to 1 V vs. OER. These high $\eta_{OER,10mA}$ may arise because the catalytic material completely corroded or became insulating during PETS treatment, or the catalytic performance of the material at pH 3 is poor. Likely, these processes occur simultaneously, as most OER-active metal oxides corrode in acid or have been demonstrated to activate an OH^--based mechanism[41,42]. Another apparent trend is that Co-rich samples tend to be good acid OER catalysts, and (Cu-Mn-Ta-Sn)O_x-rich samples have comparatively high $\eta_{OER,10mA}$ at every pH. (Cu-Mn-Ta-Fe)O_x samples show the most prominent drop in $\eta_{OER,10mA}$ between pH 7 to pH 9, followed by a smaller drop from pH 9 to pH 13.

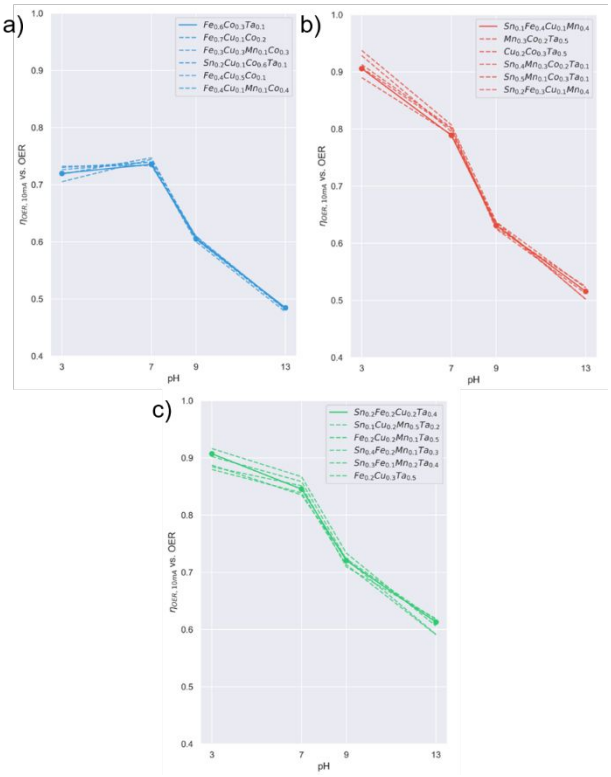

Figure 4: $\eta_{OER,10mA}$(pH) for centroid composition for every of the three identified clusters a) A, b) B, c) C with the accompanying five next nearest neighbors to the centroid. Selected compositions are compositionally distant, however functionally very similar. The selected samples contain a) 5 b) all and c) four out of six elements in the library.

The above-mentioned trends motivate clustering all samples into three clusters. Functional classification is done via clustering samples by their $\eta_{OER,10mA}$(pH) using spectral clustering with a radial Gaussian affinity kernel. All data points were standard scaled (i.e. zero mean and unit variance) prior to clustering, as is standard practice. The clustering results are shown in Figure 3b - 3d. The cluster-separated violin plots in Figure 3b demonstrate functional differences among the different classes, highlighting materials that follow the general trend of monotonic improvement of $\eta_{OER,10mA}$ with pH (cluster B) and those that break the linear trend at low or high pH (cluster C and A). It is apparent that the clusters generally exhibit an approximately-normal distribution of overpotentials at each pH with substantial overlap between clusters, particularly at high and low pH. The clusters are well separated in both the composition (Figure 3c) and property space, as shown in the 3D MDS representation of the standard scaled $\eta_{OER,10mA}$(pH) data in Figure 3e.

This functional clustering enables going beyond identification of top performers (see below) to identify representative samples for specific functions, synthesis pathways or catalyst classes. This identification is done by retrieving the centroid of each of the three functional clusters (shown in 3 b) and 3 c)) via calculating the mean position in the four dimensional $\eta_{OER,10mA}$(pH) space and selecting the six (centroid and five next nearest neighbors) samples closest (by squared euclidean distance) to the cluster center. This selection reveals samples identified via functional clustering that are emblematic of a functional cluster/class (A, B, and C). Significantly, these samples are not compositionally close (unlike top performers) but partially originate from different quaternaries and constitute six compositional 'trends', thereby highlighting the

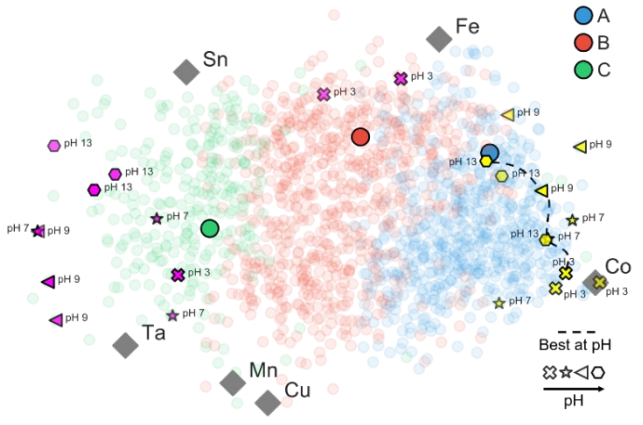

Figure 5: Proposed functional map for OER catalysts at different pH for the function and composition space (totaling over 8000 measurements). Samples are color coded according to cluster membership described above. Grey diamond shaped points mark samples with single metal compositions, yellow symbols denote the three samples with the lowest $\eta_{OER,10mA}$ at the respective pH, magenta squares the three with the highest $\eta_{OER,10mA}$ And the black dashed line denotes the top performing materials

necessity to visualize catalytic performance and cluster membership for six elements at once and not in the otherwise necessary 60 individual pseudo-quaternary diagrams.

The visualizations of overpotential and cluster membership so far has utilized MDS-based data reduction with respect to composition (Figures 2, 3c-3e) or pH (Figure 3b), and the scalability of MDS to higher input dimensions enables visualization of the combinations of these parameter spaces, i.e. a 10-dimensional parameter-space containing the standardized composition (6 dimensions for concentration of each element) and functional properties (four dimensions for each $\eta_{OER,10mA}$ measured at a different pH). The resulting 2D MDS of Figure 5 provides a functional map encoding all available composition and functional property information, as well as cluster membership, in a digestible form.

From the functional map, it is apparent that the best performing samples are rich in Co and Fe and perform well at any pH. Ta- and Sn-rich samples exhibit the highest $\eta_{OER,10mA}$ at any pH. Cluster A contains the samples with lowest $\eta_{OER,10mA}$ at any pH. From the functional maps for this composition space it would follow that an OER catalyst with good performance over a wide pH range would be found in the (Co-Mn-Cu-Fe)O_x system with alloying of SnO_x. An unfavorable choice for OER catalysts would be Ta and Sn rich systems. An interesting finding is the variety of active OER catalyst compositions at each pH.

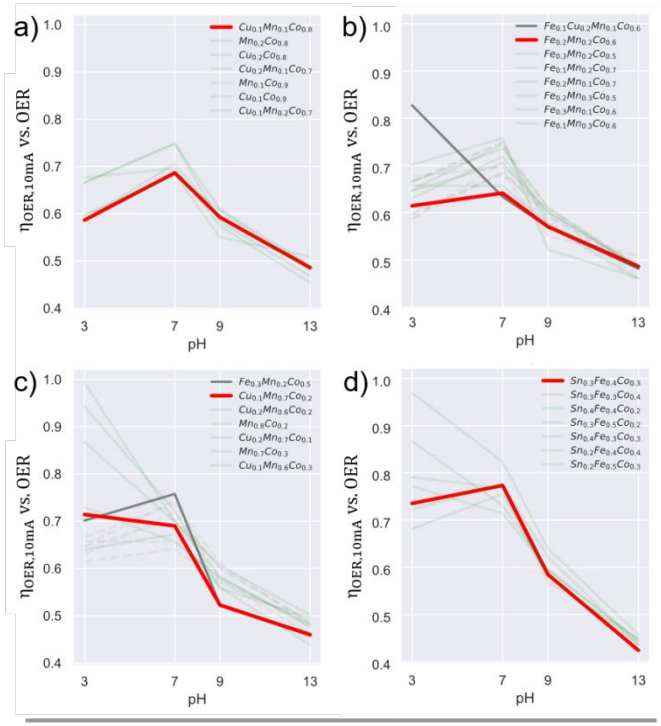

Figure 6: Samples with highest activity (lowest $_{OER,10mA}$) at selected pH are shown as red lines for pH 3-9 (a to d, respectively). At pH 7 and pH 9, the 2nd lowest overpotential sample is shown in red because the lowest overpotential samples (dark grey) is suspected of being an outlier. By non-trivial addition of certain elements, the Co-rich catalyst activity can be optimized for a specific pH at the expense of less activity at other pH.

To assess if the top performing materials are outliers, and to show the influence of alloying in close compositional vicinity, the top performers are plotted with their respective nearest composition neighbors in Figure 6. If one of the compositional nearest neighbors to the best material at a given pH is not the second best performing catalyst, the best material is treated as an outlier and the second best is chosen (in these cases, the third best is a compositional nearest neighbor of the second best, i.e. for each pH there is 0 or 1 high performance outlier). While Co is the only consistent element in the best catalysts from each pH, the concentration of Co in the best catalysts decreases with increasing pH. An intriguing result that is uniquely enabled by the high-dimensional combinatorial study is that the additional elements that optimize Co-containing catalysts vary with pH; going from acid to base, the most favorable alloying elements are Mn and Cu at pH 3, Mn and Fe at pH 7, Mn and Cu at pH 9, and Fe and Sn at pH 13. The importance of Sn at high pH is particularly surprising given that all of the metals can form stable (hydr)oxides in alkaline electrolytes, indicating that Sn may participate directly in the catalysis or alter the properties of the Co/Fe active sites, as previously observed for Ce-containing mixed metal oxides[18]. This observation is one example of the many observations that can be extracted from this large dataset to motivate and design future research to elucidate catalyst mechanisms and the role of different elements in optimizing OER catalysis.

From the functional map in Figure 5 a Co-rich catalyst family is identified that can be tuned to be a good OER catalyst in any pH by appropriate combination with a second, third or fourth cation. This pH-tailored catalyst shows an activity trend across two pseudoquaternary composition spaces that motivates further studies on the complete psuedoquinary composition space. This finding would not have been possible from a manual analysis of all 15 pseudoquaternary spaces at all four pHs (see Figure S8). The identified acid-stable catalyst performs favorably relative to a compositionally similar catalyst, $CoFePbO_x$[43].

The performance and optimal composition of this catalyst was further explored by preparing a follow-up library at 5 at% composition steps of the (Co-Cu-Mn-Sn)O_x composition space. (See ESI Figure S3) The stability and performance of the identified optimal composition was tested in pH 3 on a $Co_{0.8}Cu_{0.1}Mn_{0.1}O_x$ film deposited by ink-jet printing onto a glassy carbon electrode in an RDE setup (Figure S4). Additional high performance compositions were prepared and tested on ca. 1 cm^2 films on FTO (Figure S5), but none of the investigated compositions were stable for more than a few hours (see ESI). This is consistent with literature[44] indicating a persistent, small Co-corrosion current that does not strongly influence instantaneous measurements of overpotential, but intrinsically limits the operational lifetime. This discovery of an active catalyst of limited stability suggests alternate screening parameters i.e. PETS treatment for several days instead of hours. However, the identified pH-tunable Co-based OER catalyst family suggests interesting applications in PEC and other electrochemical energy conversion fields.

Discussion

To the best of our knowledge, our utilization of cMDS is the first to rapidly visualize a variety of composition spaces, enabling exploration of extremely large electrochemical activity datasets from the synthesized compositionally diverse combinatorial materials libraries. The cMDS as shown in Figures 1, 3, and 4 reveals interesting and novel trends in activity as a function of pH and composition. In general, OER catalysts can be categorized into three classes that are most distinctly differentiated by their high or low activity at pH 3 and 13, where almost no catalyst exhibits a comparably low $\eta_{OER,10mA}$ at all pHs. The best performing materials are typically found at 3- or 4-metal compositions, but never at the 1- or 2-metal compositions. Beyond the identification of facile composition trends, these diagrams corroborate the claim[17] that a certain degree of compositional complexity is necessary to have a well-performing OER catalyst.

Beyond the identification of top performers is identification of materials that are representative for classes of functional behavior. These compositions are identified in Figure 4 for the (Cu-Mn-Ta-Co-Sn-Fe)O_x composition space and are identified as representative of each functional class of pH-dependent OER performance. Further investigation of these compositions is expected to yield a deeper mechanistic understanding beyond what can be obtained by investigating only the top performing catalysts. We therefore refer to these samples as likely being those of highest informational relevance for subsequent studies regarding underlying mechanisms of why these classes exist.

Based on all acquired results, a combined 2D MDS-based representation of initial composition and function is generated in which every sample is represented as a 10 dimensional vector that encodes standard scaled composition and $\eta_{OER,10mA}$ at all pHs. An interesting finding is a sharp boundary between those samples belonging to class C samples, with typically high $\eta_{OER,10mA}$ at pH 13 and overall low OER activity, and the other classes.

To gather mechanistic understanding, one has to decouple stability and performance, which is often difficult in 'one-sample-at-a-time' experiments. With the abundance of a large OER catalyst dataset it is possible to deduce some mechanistic understanding. The OER catalyst data suggests that there are three catalyst classes in this composition space. The most easily understood class contains those materials that follow a monotonic trend of decreasing $\eta_{OER,10mA}$ vs. pH (Cluster B) and generally perform better at higher pH. As the potential needed to obtain a certain current density is dependent on the concentration of OH-, it is suggested that these materials catalyze the OER via adsorption of OH^-, as suggested in the classic OER reaction pathways discussed in the literature.[41,45] Another class contains the Co-rich catalysts that perform particularly well at low and neutral pH (cluster A). For these catalysts it is suggested that, depending on pH, they can catalyze the OER via direct oxidation of water (low pH) or via adsorption of OH^-. The direct oxidation of water does, however, seem to be the less favorable route since a larger overpotential is needed. The third class are those materials that show a generally high overpotential at any pH with a less than linear decrease in $\eta_{OER,10mA}$ with increasing pH; these catalysts seem to both not perform well in terms of catalytic activity and perform relatively worse in alkaline electrolytes, perhaps due to lower stability.

Conclusions

This study employed high-throughput electrochemistry to experimentally evaluate the catalytic OER performance of thousands of compositions across the pH range of 3-13. In order to comprehend the volume of data generated, data-science was leveraged to generate functional maps facilitating the use of human insight, resulting in the discovery of an precious metal-free catalyst at pH 3, identification of the pH-dependent combinations of elements that optimize Co-based catalysts, and classification of the broad range of catalyst compositions into three major classes of OER catalysts, providing insight into the underlying OER mechanisms.

Conflicts of interest

There are no conflicts to declare.

Acknowledgements

This material is based upon work performed by the Joint Center for Artificial Photosynthesis, a DOE Energy Innovation Hub, supported through the Office of Science of the U.S. Department of Energy under Award Number DE-SC0004993.

References

1 M. R. Shaner, H. A. Atwater, N. S. Lewis and E. W. McFarland, *Energy Amp Environ. Sci.*, 2016, **9**, 2354–2371.
2 R. Chaubey, S. Sahu, O. O. James and S. Maity, *Renew. Sustain. Energy Rev.*, 2013, **23**, 443–462.
3 B. Parkinson, *ACS Energy Lett.*, 2016, **1**, 1057–1059.
4 J. B. Gerken, S. E. Shaner, R. C. Massé, N. J. Porubsky and S. S. Stahl, *Energy Amp Environ. Sci.*, 2014, **7**, 2376–2382.
5 C. Xiang, A. Z. Weber, S. Ardo, A. Berger, Y. Chen, R. Coridan, K. T. Fountaine, S. Haussener, S. Hu, R. Liu, N. S. Lewis, M. A. Modestino, M. M. Shaner, M. R. Singh, J. C. Stevens, K. Sun and K. Walczak, *Angew. Chem. Int. Ed.*, 2016, **55**, 12974–12988.
6 E. Verlage, S. Hu, R. Liu, R. J. R. Jones, K. Sun, C. Xiang, N. S. Lewis and H. A. Atwater, *Energy Environ. Sci.*, 2015, **8**, 3166–3172.
7 F. Ambrosio, J. Wiktor and A. Pasquarello, *ACS Energy Lett.*, 2018, **3**, 829–834.
8 L. Zhou, A. Shinde, D. Guevarra, F. M. Toma, H. S.

Stein, J. M. Gregoire and J. A. Haber, *ACS Appl. Energy Mater.*, , DOI:10.1021/acsaem.8b01377.
9 F. Ambrosio, J. Wiktor and A. Pasquarello, *ACS Appl. Mater. Interfaces*, 2018, **10**, 10011–10021.
10 R. A. Potyrailo and V. M. Mirsky, *Chem. Rev.*, 2008, **108**, 770–813.
11 R. Potyrailo, K. Rajan, K. Stoewe, I. Takeuchi, B. Chisholm and H. Lam, *ACS Comb. Sci.*, 2011, **13**, 579–633.
12 W. F. Maier, K. Stöwe and S. Sieg, *Angew. Chem. Int. Ed.*, 2007, **46**, 6016–6067.
13 E. J. Amis, X. D. Xiang and J. C. Zhao, *MRS Bull.*
14 H. S. Stein, R. Gutkowski, A. Siegel, W. Schuhmann and A. Ludwig, *J. Mater. Chem. A*, 2016, **4**, 8, 3148-3152
15 J. M. Gregoire, D. A. Boyd, D. Guevarra, J. A. Haber, R. Jones, K. Kan, M. Marcin, P. F. Newhouse, A. Shinde, E. Soedarmadji, S. K. Suram and L. Zhou, in *Energy and Environment Series*, eds. I. D. Sharp, H. A. Atwater and H.-J. Lewerenz, Royal Society of Chemistry, Cambridge, 2018, pp. 305–340.
16 J. A. Haber, Y. Cai, S. Jung, C. Xiang, S. Mitrovic, J. Jin, A. T. Bell and J. M. Gregoire, *Energy Amp Environ. Sci.*, 2014, **7**, 682–688.
17 J. A. Haber, C. Xiang, D. Guevarra, S. Jung, J. Jin and J. M. Gregoire, *ChemElectroChem*, 2013, **1**, 524–528.
18 M. Favaro, W. S. Drisdell, M. A. Marcus, J. M. Gregoire, E. J. Crumlin, J. A. Haber and J. Yano, *ACS Catal.*, 2017, **7**, 1248–1258.
19 C. Schwanke, H. S. Stein, L. Xi, K. Sliozberg, W. Schuhmann, A. Ludwig and K. M. Lange, *Sci. Rep.*, 2017, **7**, 44192.
20 R. J. R. Jones, A. Shinde, D. Guevarra, C. Xiang, J. A. Haber, J. Jin and J. M. Gregoire, *ACS Comb. Sci.*, 2015, **17**, 71–75.
21 J. M. Gregoire, C. Xiang, X. Liu, M. Marcin and J. Jin, *Rev. Sci. Instrum.*, 2013, **84**, 24102–24107.
22 C. Suh, S. C. Sieg, M. J. Heying, J. H. Oliver, W. Maier and K. Rajan, 2009, **11**, 385–392.
23 S. J. Campbell, A. Gaulton, J. Marshall, D. Bichko, S. Martin, C. Brouwer and L. Harland, *Drug Discov. Today*, 2010, **15**, 3–15.
24 K. Daniels, G. Grinstein, A. Russell and M. Glidden, *Inf. Vis.*, 2012, **11**, 273–300.
25 Y. J. Li, A. Savan, A. Kostka, H. S. Stein and A. Ludwig, *Mater. Horiz.*, **5**, 86-92
26 J. B. Kruskal, *Psychometrika*, 1964, **29**, 115–129.
27 L. van der Maaten, *J. Mach. Learn. Res.*, 2014, **15**, 3221–3245.
28 S. Ermon, R. Le Bras, S. K. Suram, J. M. Gregoire, C. P. Gomes, B. Selman and R. B. van Dover, 2015.
29 S. Ermon, R. Le Bras, C. P. Gomes, B. Selman and R. B. van Dover, in *Theory and Applications of Satisfiability Testing – SAT 2012*, Springer Berlin Heidelberg, Berlin, Heidelberg, 2012, vol. 7317, pp. 172–185.
30 H. S. Stein, S. Jiao and A. Ludwig, *ACS Comb. Sci.*, 2017, **19**, 1, 1-8
31 D. Guevarra, A. Shinde, S. K. Suram, I. D. Sharp, F. M. Toma, J. A. Haber and J. M. Gregoire, *Energy Environ. Sci. 2016, 9, 565–580*.
32 X. Liu, Y. Shen, R. Yang, S. Zou, X. Ji, L. Shi, Y. Zhang, D. Liu, L. Xiao, X. Zheng, S. Li, J. Fan and G. D. Stucky, *Nano Lett.*, 2012, **12**, 5733–5739.
33 A. Shinde, R. J. R. Jones, D. Guevarra, S. Mitrovic, N. Becerra-Stasiewicz, J. A. Haber, J. Jin and J. M. Gregoire, *Electrocatalysis*, 2014, **6**, 229–236.
34 A. Shinde, S. K. Suram, Q. Yan, L. Zhou, A. K. Singh, J. Yu, K. A. Persson, J. B. Neaton and J. M. Gregoire, *ACS Energy Lett.*, 2017, 2307–2312.
35 M. Pourbaix, *Atlas of electrochemical equilibria in aqueous solutions*, Natl. Assn. of Corrosion Engineers, 1974.
36 E. D. Verink JR., *Corrosion*, 1967, **23**, 371–373.
37 M. R. Nellist, F. A. L. Laskowski, F. Lin, T. J. Mills and S. W. Boettcher, *Acc. Chem. Res.*, 2016, **49**, 733–740.
38 F. Lin and S. W. Boettcher, *Nat. Mater.*, 2014, **13**, 81–86.
39 M. E. G. Lyons, R. L. Doyle and M. P. Brandon, *Phys. Chem. Chem. Phys.*, 2011, **13**, 21530.
40 A. Grimaud, O. Diaz-Morales, B. Han, W. T. Hong, Y.-L. Lee, L. Giordano, K. A. Stoerzinger, M. T. M. Koper and Y. Shao-Horn, *Nat. Chem.*, 2017, **9**, 457–465.
41 J. O. Bockris and T. Otagawa, *J. Phys. Chem.*, 1983, **87**, 2960–2971.
42 J. O. Bockris, E. H. Crook, H. Bloom and N. E. Richards, *Proc. R. Soc. Math. Phys. Eng. Sci.*, 1960, **255**, 558–578.
43 M. Huynh, T. Ozel, C. Liu, E. C. Lau and D. G. Nocera, *Chem. Sci.*, 2017, **8**, 4779–4794.
44 D. Seley, K. Ayers and B. A. Parkinson, *ACS Comb. Sci.*, 2013, **15**, 82–89.
45 I. C. Man, H. Y. Su, F. Calle Vallejo, H. A. Hansen, J. I. Martínez, N. G. Inoglu, J. Kitchin, T. F. Jaramillo, J. K. Nørskov and J. Rossmeisl, *ChemCatChem*, 2011, **3**, 1159–1165.